INTERNATIONAL JOURNAL FOR NUMERICAL METHODS IN FLUIDS
Int. J. Numer. Meth. Fluids 2009; **59**:767–790
Published online 9 July 2008 in Wiley InterScience (www.interscience.wiley.com). DOI: 10.1002/fld.1837

Impact of mass lumping on gravity and Rossby waves in 2D finite-element shallow-water models

D. Y. Le Roux[1,*,†], E. Hanert[2], V. Rostand[1] and B. Pouliot[1]

[1]*Département de Mathématiques et de Statistique, Université Laval, Québec, Que., Canada G1K 7P4*
[2]*Department of Meteorology, The University of Reading, Earley Gate, P.O. Box 243, Reading RG6 6BB, U.K.*

SUMMARY

The goal of this study is to evaluate the effect of mass lumping on the dispersion properties of four finite-element velocity/surface-elevation pairs that are used to approximate the linear shallow-water equations. For each pair, the dispersion relation, obtained using the mass lumping technique, is computed and analysed for both gravity and Rossby waves. The dispersion relations are compared with those obtained for the consistent schemes (without lumping) and the continuous case. The $P_0 - P_1$, RT_0 and $P_1^{\mathrm{NC}} - P_1$ pairs are shown to preserve good dispersive properties when the mass matrix is lumped. Test problems to simulate fast gravity and slow Rossby waves are in good agreement with the analytical results. Copyright © 2008 John Wiley & Sons, Ltd.

Received 20 July 2007; Revised 14 February 2008; Accepted 30 March 2008

KEY WORDS: shallow-water equations; finite elements; mass lumping; gravity waves; Rossby waves

1. INTRODUCTION

The shallow-water (SW) equations are the simplest geophysical flow model allowing the existence of fast gravity and slow Rossby waves. These equations can be derived from the Navier–Stokes equations expressed in a rotating frame of reference by integrating them over the depth of the fluid layer and assuming a small aspect ratio. Owing to their inherent simplicity, while still retaining some of the main driving forces of geophysical flows, the SW equations are often used as a benchmark for numerical schemes to be used in more complex oceanic or atmospheric models. The simulation of gravity waves allows one to assess the model's ability to represent phenomena such as tsunamis or mountain waves. On a larger scale, slow Rossby waves play an important role

*Correspondence to: D. Y. Le Roux, Département de Mathématiques et de Statistique, Université Laval, Québec, Que., Canada G1K 7P4.
†E-mail: Daniel.LeRoux@mat.ulaval.ca, dleroux@mat.ulaval.ca

Contract/grant sponsor: Natural Sciences and Engineering Research Council (NSERC)

in the global circulation of both the atmosphere and the ocean, and thus on climate as a whole. Any model designed for climatic applications should simulate them accurately.

The finite-element (FE) method is one of the many numerical methods available to solve the SW equations [1–7]. Its main advantage lies in the possibility of discretizing the equations on unstructured meshes. Such meshes offer the enhanced flexibility of variable resolution and elements' shape and orientation for representing localized phenomena in complex domains. One of the disadvantages of the method is that the Galerkin formulation usually introduces a non-diagonal mass matrix that multiplies the temporal derivative of the space-discretized solution. The solution of the discrete system of algebraic equations therefore requires the inversion of that non-diagonal mass matrix regardless of the time integration scheme. This means that even an explicit time integration scheme usually requires the use of a linear solver to obtain the solution at each time step. As a result, the computational cost of an explicit FE model is usually much higher than the one of an equivalent finite-difference model.

The so-called mass lumping technique has been introduced to improve FE schemes' efficiency by diagonalizing the mass matrix. Two techniques have been suggested to perform that diagonalization. The first one amounts to add the off-diagonal elements to the diagonal elements of the consistent mass matrix so that the total 'mass' associated with a node is conserved [8]. Another approach, suggested by Fried and Malkus [9], amounts to use an inexact numerical integration rule where integration nodes coincide with the nodes of the element. Since all but one shape function are zero at a given node, the resulting mass matrix is diagonal.

In ocean and atmosphere FE models, the mass lumping procedure is often used to improve the efficiency of the model and to achieve computational performances comparable to those of finite-difference models. The impact of this procedure on the model accuracy has not been thoroughly investigated yet with the exception of some early work by Foreman [10]. In this study, we aim to focus on the dispersion properties of several lumped FE schemes for both gravity and Rossby waves. This work builds upon recent studies by Le Roux *et al.* [11–15], which have compared the dispersion relations of a number of low-order FE models of the SW equations. They have shown that the coupling between the discrete momentum and continuity equations could lead to some serious phase and group velocity errors for both gravity and Rossby waves. Only a few FE schemes are able to maintain good accuracy and thus appear to be suitable for geophysical applications. The effect of mass lumping on the accuracy of four FE pairs is investigated in the present study.

The outline of the paper is the following. The model equations and free modes are presented in Section 2. The spatial discretization follows in Section 3. In Section 4, the computation of the lumped dispersion relations are performed for the four FE pairs for both gravity and Rossby waves. These dispersion relations are compared analytically and graphically with the continuous case in Section 5. The dispersion analysis is followed by two numerical tests in Section 6. Some concluding remarks complete the study.

2. GOVERNING EQUATIONS AND FREE MODES

The inviscid linear SW equations are expressed in Cartesian coordinates [16] as

$$\bar{\mathbf{u}}_t + f\mathbf{k}\times\bar{\mathbf{u}} + g\nabla\bar{\eta} = 0 \tag{1}$$

$$\bar{\eta}_t + H\nabla\cdot\bar{\mathbf{u}} = 0 \tag{2}$$

DOI: 10.1002/fld

where $\bar{\mathbf{u}}=(\bar{u},\bar{v})$ is the velocity field, $\bar{\eta}$ is the surface elevation with respect to the reference level $z=0$, g and f are the gravitational acceleration and Coriolis parameter, respectively; $\mathbf{k}$ is a unit vector in the vertical direction and the mean depth H is assumed constant. For a contained flow, (1) and (2) are solved subject to the no-normal flow boundary condition $\bar{\mathbf{u}}\cdot\mathbf{n}=0$ on the boundary Γ of the domain Ω, where $\mathbf{n}$ is the outward pointing normal on Γ. We now examine the free modes of (1) and (2) corresponding to inertia-gravity and Rossby waves.

2.1. Inertia-gravity waves

For this analysis we seek periodic solutions of (1)–(2) of the form

$$\bar{\mathbf{u}}(x,y,t)=\mathbf{u}(x,y)\mathrm{e}^{-\mathrm{i}\omega t},\quad \bar{\eta}(x,y,t)=\eta(x,y)\mathrm{e}^{-\mathrm{i}\omega t} \tag{3}$$

where $\mathbf{u}=(u,v)$ and η are amplitudes, and ω is the angular frequency. Equations (1) and (2) then reduce to

$$-\mathrm{i}\omega\mathbf{u}+f\mathbf{k}\times\mathbf{u}+g\nabla\eta=0 \tag{4}$$

$$-\mathrm{i}\omega\eta+H\nabla\cdot\mathbf{u}=0 \tag{5}$$

The free modes of (4)–(5) are examined by perturbing about the basic state $u=v=\eta=0$. Because the governing equations are linear, the solution may be examined by considering the behaviour of one Fourier mode. We then seek solutions of (4)–(5) of the form $(u,v,\eta)=(\tilde{u},\tilde{v},\tilde{\eta})\,\mathrm{e}^{\mathrm{i}(kx+ly)}$, where k and l are the wave numbers in the x- and y-directions, respectively. Substitution into (4)–(5) leads to a square matrix system for the amplitudes $\tilde{u},\tilde{v},\tilde{\eta}$. For a non-trivial solution to exist, the determinant of the matrix must equal zero, and this leads to the so-called dispersion relation for the frequency

$$\omega(\omega^2-f^2-gH(k^2+l^2))=0 \tag{6}$$

The first solution $\omega=0$ is the geostrophic mode, while the other two solutions

$$\omega_{\mathrm{AN}}^{\mathrm{G}}=\pm\sqrt{f^2+gH(k^2+l^2)} \tag{7}$$

correspond to the free-surface gravitational modes with rotational correction. Since ω is purely real, all modes are neutrally stable and neither amplify nor decay.

2.2. Rossby waves

Here, we do not neglect the Coriolis force and the β-plane approximation, $f=f_0+\beta y$, is used [17]. As for the gravity waves we seek periodic solutions and we obtain

$$-\mathrm{i}\omega\mathbf{u}+(f_0+\beta y)\mathbf{k}\times\mathbf{u}+g\nabla\eta=0 \tag{8}$$

$$-\mathrm{i}\omega\eta+H\nabla\cdot\mathbf{u}=0 \tag{9}$$

Equations (8) and (9) will govern the planetary wave motion due to the variation in the Coriolis parameter with latitude. In (8) and (9), the larger terms (f_0, g and H) govern the steady geostrophic dynamics, whereas the smaller ones (the time derivatives and the β term) may be considered as

DOI: 10.1002/fld

perturbations and, although small, govern the wave evolution. In the first approximation, the large terms dominate and the motion is called geostrophic. From (8) we obtain

$$\mathbf{u} \simeq \frac{g}{f_0}\,\mathbf{rot}\,\eta \tag{10}$$

with $\mathbf{rot}\,\eta \equiv (-\eta_y, \eta_x)$. Using (10) in the small terms of (8) yields

$$-\mathrm{i}\omega\frac{g}{f_0}\,\mathbf{rot}\,\eta + f_0\mathbf{k}\times\mathbf{u} + \frac{g}{f_0}\beta y\mathbf{k}\times\mathbf{rot}\,\eta + g\nabla\eta = 0 \tag{11}$$

and we deduce

$$\mathbf{u} = \frac{g}{f_0}\,\mathbf{rot}\,\eta + \mathrm{i}\omega\frac{g}{f_0^2}\nabla\eta - \frac{g}{f_0^2}\beta y\,\mathbf{rot}\,\eta \tag{12}$$

In the right-hand side of (12) the first term is identified as the geostrophic velocity and the next and small terms represent the ageostrophic motion. Final substitution of $\mathbf{u}$ from (12) in the continuity equation (9) leads to a linear equation with constant coefficients

$$\mathrm{i}\omega(\eta - \lambda^2\nabla^2\eta) + \beta\lambda^2\eta_x = 0 \tag{13}$$

where $\lambda \equiv \sqrt{gH}/f_0$ is the deformation radius. We then seek solutions of the form $\eta = \tilde{\eta}\mathrm{e}^{\mathrm{i}(kx+ly)}$ and their substitution into (13) leads to the so-called dispersion relation for the frequency

$$\omega_{\mathrm{AN}}^{\mathrm{R}} = \frac{-\beta k}{\lambda^{-2} + k^2 + l^2} \tag{14}$$

The relation (14) may be viewed as a particular case of the Longuet-Higgins approach [18] and has been introduced by Wentzel in [19].

3. SPATIAL DISCRETIZATION

3.1. The weak formulation

3.1.1. Inertia-gravity waves. We assume that $\mathbf{u}$ and η belong to either the square-integrable space $L^2(\Omega)$ or the Sobolev space $H^1(\Omega)$, i.e. the space of functions in $L^2(\Omega)$ whose first derivatives belong to $L^2(\Omega)$. The weak formulation of (4) and (5) requires the test functions $\boldsymbol{\varphi}$ (whose x- or y-component is formally denoted by φ) and ψ to be sufficiently regular and to, respectively, belong to the same function space as $\mathbf{u}$ and η, such that

$$-\mathrm{i}\omega\int_\Omega \mathbf{u}\cdot\boldsymbol{\varphi}\,\mathrm{d}\Omega + \int_\Omega f(\mathbf{k}\times\mathbf{u})\cdot\boldsymbol{\varphi}\,\mathrm{d}\Omega + g\int_\Omega \nabla\eta\cdot\boldsymbol{\varphi}\,\mathrm{d}\Omega = 0 \tag{15}$$

$$-\mathrm{i}\omega\int_\Omega \eta\psi\,\mathrm{d}\Omega + H\int_\Omega \nabla\cdot\mathbf{u}\psi\,\mathrm{d}\Omega = 0 \tag{16}$$

where $\mathrm{d}\Omega$ is the area element.

Depending on the regularity of $\mathbf{u}$ and η, the terms containing derivatives in (15) and (16) may be integrated by parts using Green's theorem. In that case, (15) can be rewritten as

$$\mathrm{i}\omega\int_\Omega \mathbf{u}\cdot\boldsymbol{\varphi}\,\mathrm{d}\Omega - \int_\Omega f(\mathbf{k}\times\mathbf{u})\cdot\boldsymbol{\varphi}\,\mathrm{d}\Omega + g\int_\Omega \eta\nabla\cdot\boldsymbol{\varphi}\,\mathrm{d}\Omega = 0 \tag{17}$$

DOI: 10.1002/fld

and for (16) we obtain

$$\mathrm{i}\omega \int_\Omega \eta\psi \,\mathrm{d}\Omega + H \int_\Omega \mathbf{u}\cdot\nabla\psi \,\mathrm{d}\Omega = 0 \tag{18}$$

by letting $\mathbf{u}\cdot\mathbf{n}=0$ (and $\boldsymbol{\varphi}\cdot\mathbf{n}=0$) on Γ.

3.1.2. Rossby waves. The weak formulation of (12) and (9) leads to

$$\int_\Omega \mathbf{u}\cdot\boldsymbol{\varphi}\,\mathrm{d}\Omega = \frac{g}{f_0}\int_\Omega \mathbf{rot}\,\eta\cdot\boldsymbol{\varphi}\,\mathrm{d}\Omega + \mathrm{i}\omega\frac{g}{f_0^2}\int_\Omega \nabla\eta\cdot\boldsymbol{\varphi}\,\mathrm{d}\Omega - \frac{g\beta}{f_0^2}\int_\Omega y\,\mathbf{rot}\,\eta\cdot\boldsymbol{\varphi}\,\mathrm{d}\Omega \tag{19}$$

$$-\mathrm{i}\omega\int_\Omega \eta\psi\,\mathrm{d}\Omega + H\int_\Omega \nabla\cdot\mathbf{u}\psi\,\mathrm{d}\Omega = 0 \tag{20}$$

Depending on the regularity of $\mathbf{u}$ and η, the terms containing derivatives in (19) and (20) may be integrated by parts using Green's theorem. In that case, (19) can be rewritten as

$$\int_\Omega \mathbf{u}\cdot\boldsymbol{\varphi}\,\mathrm{d}\Omega = -\frac{g}{f_0}\int_\Omega \eta\,\mathrm{rot}\,\boldsymbol{\varphi}\,\mathrm{d}\Omega - \mathrm{i}\omega\frac{g}{f_0^2}\int_\Omega \eta\nabla\cdot\boldsymbol{\varphi}\,\mathrm{d}\Omega + \frac{g\beta}{f_0^2}\int_\Omega \eta\,\mathrm{rot}(y\boldsymbol{\varphi})\,\mathrm{d}\Omega \tag{21}$$

by letting $\mathbf{u}\cdot\mathbf{n}=0$ on Γ and $\mathrm{rot}\,\mathbf{u}\equiv v_x - u_y$. For (20) we obtain

$$\mathrm{i}\omega\int_\Omega \eta\psi\,\mathrm{d}\Omega + H\int_\Omega \mathbf{u}\cdot\nabla\psi\,\mathrm{d}\Omega = 0 \tag{22}$$

3.2. Galerkin FE discretization

The Galerkin FE method approximates the solution of (15)–(16) and (19)–(20), and eventually (17)–(18) and (21)–(22) if integration by parts needs to be performed, in finite-dimensional subspaces. Let us consider a FE triangulation $\mathscr{T}_h$ of the polygonal domain Ω, where h is a representative meshlength parameter that measures resolution. For a triangle $K\in\mathscr{T}_h$, let $P_s(K)$ denote the space of polynomials of degree s on K. The discrete solutions $\mathbf{u}_h$ and η_h belong to finite-dimensional spaces whose restrictions on K belong to $P_q(K)\times P_q(K)$ for $\mathbf{u}_h$ and to $P_r(K)$ for η_h. The components of $\mathbf{u}_h$ and η_h are represented over K by interpolating functions. Introducing the FE basis leads to a FE statement as in (15)–(16) and (19)–(20), and eventually in (17)–(18) and (21)–(22), but with $\mathbf{u},\eta$ replaced by the FE trial functions $\mathbf{u}_h,\eta_h$ and φ,ψ replaced by the corresponding FE test functions.

3.3. The FE pairs

Four candidate FE pairs for representing velocity and surface elevation are described and evaluated in the remainder of this study. In Figure 1, velocity and surface-elevation node locations are represented by the symbols ● and ○, respectively, for the pairs. The black arrows indicate the location of normal velocity nodes, and the arrow points in the direction of the chosen normal. The conventional nomenclature $P_q - P_r$ means that velocity and surface elevation are, respectively, represented as piecewise-defined polynomials of degree q and r. Enhancements of this basic terminology are introduced as needed.

The RT_0 element, also called low-order Raviart–Thomas element [20], has a discontinuous piecewise-constant representation of surface elevation. It is based on flux conservation on element

DOI: 10.1002/fld

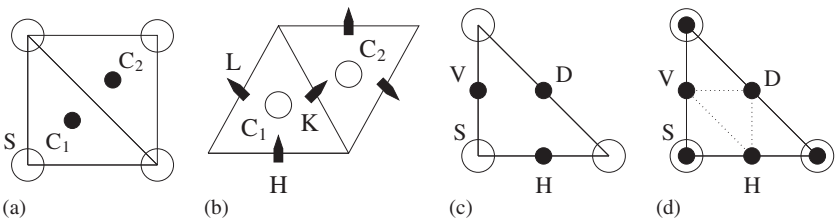

Figure 1. Velocity and surface-elevation node locations are represented by the symbols ● and ○, respectively, for the (a) P_0-P_1, (b) RT_0, (c) $P_1^{\mathrm{NC}}-P_1$, and (d) P_1 iso P_2-P_1 pairs. The black arrows indicate the location of normal velocity nodes, and the arrow points in the direction of the chosen normal. The capital letters refer to the typical velocity and elevation nodes used in Section 4.

edges and has normal velocity components at triangle edge midpoints. Equations (16) and (17) are used to compute the inertia-gravity waves and the Rossby modes are obtained from (20) and (21). Common to the remaining FE velocity/surface-elevation pairs is a piecewise-linear continuous representation of surface elevation and they differ from one another in their representation of velocity. The $P_1^{\mathrm{NC}}-P_1$ pair [12, 21] has velocity nodes at triangle edge midpoints and linear basis functions are used to approximate the two velocity components on the element's two-triangle support. Such a representation is only continuous across triangle boundaries at midpoint nodes, and discontinuous everywhere else around a triangle boundary. As a consequence of the orthogonality property of the linear P_1^{NC} basis functions, the velocity mass matrix is 'naturally' diagonal. The P_1 iso P_2-P_1 element pair [22] has piecewise-linear basis functions for velocity on a refined triangulation obtained by dividing each triangle into four subtriangles using triangle edge midpoints. There are thus six velocity nodes over each unrefined triangle, the same as for a quadratic approximation of velocity, termed P_2. Finally, the P_0-P_1 pair [13, 14, 23] has a piecewise-constant representation of velocity. For both the $P_1^{\mathrm{NC}}-P_1$ and P_0-P_1 pairs, Equations (15) and (18) are employed to compute the inertia-gravity waves and the Rossby modes are obtained from (19) and (22).

4. COMPUTATION OF THE LUMPED DISPERSION RELATIONS

In the remainder of this study we analyse the impact of the so-called mass lumping technique on the dispersion relation for both gravity and Rossby waves using the four FE schemes described above. In order to compute the dispersion relation we follow the same procedure as in Section 2 for the continuous case, but at the discrete level. The resulting discrete momentum and continuity equations (and dispersion relations) are obtained in [13, 15] for the gravity waves and in [14] for the Rossby waves, without the use of mass lumping techniques. For the Rossby waves only the P_0-P_1 and $P_1^{\mathrm{NC}}-P_1$ pairs are considered in [14] because the velocity mass matrix needs to be diagonal in order to be able to substitute the velocity nodal values from (19) in (20), or from (21) in (22) when integration by parts is performed. This is why only FE pairs leading to 'naturally' diagonal mass matrices have been considered in [14]. In this study, in addition to the pairs examined in [14] for the Rossby waves, we also consider the RT_0 and P_1 iso P_2-P_1 pairs, via the mass lumping technique.

DOI: 10.1002/fld

For each pair, the discrete momentum and continuity equations are first obtained from the stencils of Figures 3.1, 3.2 and 3.5 in [13] and Figures 4 and 5 in [15]. The mass lumping procedure is then employed for both the velocity and elevation mass matrices.

For the P_0-P_1 and $P_1^{NC}-P_1$ pairs, the velocity mass matrices are 'naturally' diagonal. This is due to the orthogonality property of the non-conforming basis functions for the latter pair, as mentioned in Section 3.3. Consequently, the lumping procedure only needs to be performed for the P_1 elevation mass matrix for these pairs. For the P_1 iso P_2-P_1 pair, both the P_1 velocity and elevation mass matrices are lumped, and the lumping technique is applied on the refined triangulation for the velocity mass matrix. Two techniques are usually used to perform the mass lumping procedure for the P_1 element. The first approach consists in adding the off-diagonal elements to the diagonal elements of the consistent mass matrix so that the total 'mass' associated with a node is conserved [8]. If we let M and $\tilde{M}$ the consistent and lumped mass matrices, respectively, we have $\tilde{M}_{ij}=(\sum_k M_{ik})\delta_{ij}$, where δ_{ij} is the Kronecker delta. Secondly, mass lumping may be achieved by introducing reduced or inexact quadrature rules for the numerical evaluation of integrals over a triangle K of $\mathscr{T}_h$, where the sampling points coincide with the nodes of the element [9]. In the case of the P_1 element, let $(0,0)$, $(1,0)$ and $(0,1)$ denote, for example, the vertices of triangle K. The use of the trapezoidal quadrature rule $\int_K f(x,y)\,\mathrm{d}x\,\mathrm{d}y \approx \frac{1}{6}(f(0,0)+f(1,0)+f(0,1))$ leads to a diagonal mass matrix since all but one shape function are zero at a given node. Note that for the P_1 element, the use of the first approach and the trapezoidal quadrature rule technique lead essentially to the same result.

For the RT_0 element, the elevation is constant per triangle and the corresponding mass matrix is hence 'naturally' diagonal. The mass lumping technique for the velocity mass matrix requires that triangles K of $\mathscr{T}_h$ satisfy the Delaunay property, as shown in [24]. In this case, let e_j be the interior edge associated with the normal velocity component at triangle edge midpoint j. Following [24], the non-zero element corresponding to line j of the lumped matrix is $(\cot\theta_{j,1}+\cot\theta_{j,2})/2$, where $\theta_{j,1}$ and $\theta_{j,2}$ are the angles opposite of e_j.

The dispersion analysis is performed on Mesh 1, made up of biased right isosceles triangles for both the gravity and Rossby waves, except for the RT_0 pair. Mesh 2, corresponding to equilateral triangles (with horizontal faces), is used for the RT_0 scheme and the dispersion relations are also obtained for the $P_1^{NC}-P_1$ pair on Mesh 2 for comparison purposes. For the RT_0 element, we thus have $\theta_{j,1}=\theta_{j,2}=\pi/3$. The mesh spacing h is defined as the triangle side length for Mesh 2 and the shortest triangle side length for Mesh 1. Because nodal unknowns may be located on different types of nodes: vertices, faces and barycentres, selected momentum and continuity discrete equations for each type of nodes are retained. For example, three discrete momentum equations are considered for the RT_0 pair on the three possible types of faces, denoted by H (horizontal), K and L (ordered counter-clockwise), of a triangle of Mesh 2, and two discrete continuity equations are retained at the two possible types of barycentres corresponding to upward (C_1) and downward (C_2) pointing triangles as shown in Figure 1(b). For simplicity, C_1 and C_2 are also used on Mesh 1 to denote the lower left and upper right triangles, respectively, as shown in Figure 1(a) for the P_0-P_1 pair. For the $P_1^{NC}-P_1$ and P_1 iso P_2-P_1 pairs three types of faces, denoted by H (horizontal), V (vertical) and D (diagonal) are considered on Mesh 1, but only one discrete continuity equation is retained at a typical vertex node (S) as shown in Figure 1(c) and (d). For the P_1 iso P_2-P_1 pair, one additional discrete momentum equation needs to be considered at S (see Figure 1(d)). Further details are given in [12] for the $P_1^{NC}-P_1$ pair. Note that for all pairs, the typical nodes belonging to the same set are distributed on a regular grid.

DOI: 10.1002/fld

As for the continuum case, the dispersion relations for the discrete schemes are found through a Fourier expansion. The discrete solutions corresponding to $(u_j, v_j, \eta_j) = (\tilde{u}, \tilde{v}, \tilde{\eta})e^{i(kx_j+ly_j)}$ are sought at node j $(j=1,2,3,\ldots)$, where (u_j, v_j, η_j) are the nodal unknowns that appear in the selected discrete equations and $(\tilde{u}, \tilde{v}, \tilde{\eta})$ are the amplitudes. The (x_j, y_j) coordinates are expressed in terms of a distance to a reference node. Substitution in the discrete equations leads to a matrix system for the Fourier amplitudes. The dispersion relation is then obtained by setting the determinant of the matrix system to zero. For Rossby waves and FE pairs having a piecewise-linear continuous representation of surface elevation, a single equation is obtained for the Fourier amplitude and the dispersion relation is computed in a straightforward manner. Because the velocity field needs to be substituted from (19) in (20) for such waves, or from (21) in (22) if integration by parts is performed, the dispersion relation is obtained after very long and tedious algebra, and only the result is given here. Further details are found in [14].

As mentioned in [13], a realistic value of f would have little effect on the dispersion relations of the P_0-P_1, $P_1^{NC}-P_1$ and P_1 iso P_2-P_1 pairs for inertia-gravity waves when $\lambda/h \gg 1$ (high resolution). In the case $\lambda/h \ll 1$ (coarse resolution), the results are roughly preserved but at smaller scales. Further, the mass lumping technique employed for the RT_0 element does not apply to the Coriolis operator. This is why we set $f=0$ in (15), and eventually in (17), and compute the dispersion relations for pure gravity waves. The effect of the Coriolis factor is evaluated when studying the discrete dispersion relations for the slow Rossby modes.

Let I_n be the $n \times n$ identity matrix, N an $m \times n$ matrix with m and n two positive integers, $N^* = \overline{N}^T$ the conjugate transpose of N, and $A = -i\omega I_2$. We now examine the calculation of the dispersion relations for the four FE pairs that are considered in this study by using the mass lumping technique for gravity and Rossby waves.

4.1. The P_0-P_1 pair

4.1.1. Gravity modes. On Mesh 1, the selected discrete equations are expressed in the matrix form

$$\begin{pmatrix} A & 0 & \\ 0 & A & -gB^* \\ & HB & -2i\omega \end{pmatrix} \begin{pmatrix} \tilde{\mathbf{u}}_{C_1} \\ \tilde{\mathbf{u}}_{C_2} \\ \tilde{\boldsymbol{\eta}}_S \end{pmatrix} = 0 \tag{23}$$

where $B = 1/h(b_1 \;\; b_2 \;\; -\overline{b}_1 \;\; -\overline{b}_2)$, with

$$b_1 = e^{i(k+l)h/3}(1-e^{-ikh}), \quad b_2 = e^{i(k+l)h/3}(1-e^{-ilh})$$

By setting the determinant of the 5×5 system matrix in (23) to zero, we obtain $\omega_{1,2,3} = 0$ and

$$\omega_{4,5} = \pm\sqrt{2\frac{gH}{h^2}(2-\cos kh-\cos lh)} \tag{24}$$

For infinitesimal mesh spacing the frequencies $\omega_{4,5}$ coincide with the continuous solution obtained from (6) in the limit as mesh spacing $h \to 0$ and we have $\omega_{4,5} = \omega_{AN}^G + O(h^2)$.

4.1.2. Rossby modes. We let

$$a_1 = 2\sin kh + \sin lh + \sin(k-l)h, \quad a_2 = 12(2-\cos kh-\cos lh)$$

DOI: 10.1002/fld

and $r \equiv h/2\lambda$, and on Mesh 1 we obtain

$$\frac{\omega}{\beta h} = \frac{-2a_1}{24r^2 + a_2} \tag{25}$$

For infinitesimal mesh spacing we have

$$\omega = \omega_{\mathrm{AN}}^{\mathrm{R}} + O(h^2) \tag{26}$$

4.2. *The* RT_0 *pair*

For that FE scheme, the dispersion relation is only computed on Mesh 2 for both gravity and Rossby modes, and the mass lumping technique used in [24] is adopted.

4.2.1. Gravity modes. The discrete equations lead to the following system:

$$\begin{pmatrix} -\mathrm{i}\omega\dfrac{\sqrt{3}}{3} I_3 & -gB^* \\ HB & -\mathrm{i}\omega\dfrac{\sqrt{3}}{4} I_2 \end{pmatrix} \begin{pmatrix} \tilde{\mathbf{J}} \\ \tilde{\boldsymbol{\eta}} \end{pmatrix} = 0 \tag{27}$$

where $\tilde{\mathbf{J}} = (\tilde{J}_H, \tilde{J}_K, \tilde{J}_L)$ and J_p is the velocity flux through the edge containing node p (here H, K or L), with $J_p = \tilde{J}_p \mathrm{e}^{\mathrm{i}(kx_p + ly_p)}$. We also have $\tilde{\boldsymbol{\eta}} = (\tilde{\eta}_{C_1}, \tilde{\eta}_{C_2})$,

$$B = \frac{1}{h} \begin{pmatrix} -\overline{b}_1 & b_2 & -\overline{b}_3 \\ b_1 & -\overline{b}_2 & b_3 \end{pmatrix}$$

and

$$b_1 = \mathrm{e}^{\mathrm{i}\sqrt{3}lh/6}, \quad b_2 = \mathrm{e}^{\mathrm{i}(k + l/\sqrt{3})h/4}, \quad b_3 = \mathrm{e}^{\mathrm{i}(k - l/\sqrt{3})h/4}$$

For a non-trivial solution to exist, the 5×5 determinant of the coefficient matrix above must vanish. This condition implies $\omega_1 = 0$ and four additional roots corresponding to gravity modes

$$\omega_{2,3} = \pm 2 \sqrt{\frac{gH}{h^2} \left(3 - \sqrt{4 \cos\frac{kh}{2} \left(\cos\frac{kh}{2} + \cos\frac{\sqrt{3}lh}{2} \right) + 1} \right)} \tag{28}$$

$$\omega_{4,5} = \pm 2 \sqrt{\frac{gH}{h^2} \left(3 + \sqrt{4 \cos\frac{kh}{2} \left(\cos\frac{kh}{2} + \cos\frac{\sqrt{3}lh}{2} \right) + 1} \right)} \tag{29}$$

For infinitesimal mesh spacing we have

$$\omega_1 = 0, \quad \omega_{2,3} = \omega_{\mathrm{AN}}^{\mathrm{G}} + O(h^2), \quad \omega_{4,5} = \pm 2\sqrt{6} \frac{\sqrt{gH}}{h} + O(h)$$

Note that only $\omega_{2,3}$ coincide with the continuous solution obtained from (6) in the limit as mesh spacing $h \to 0$, while $\omega_{4,5}$ presumably correspond to spurious modes from the RT_0 discretization scheme.

DOI: 10.1002/fld

4.2.2. Rossby modes. We let

$$a_1=\sin\frac{kh}{2},\quad a_2=2\cos\frac{kh}{2}+\cos\frac{\sqrt{3}lh}{2}$$

$$a_3=\sin\frac{\sqrt{3}lh}{2},\quad a_4=1+4\cos\frac{kh}{2}\left(\cos\frac{kh}{2}+\cos\frac{\sqrt{3}lh}{2}\right)$$

and obtain

$$\frac{\omega_{1,2}}{\beta h}=\frac{a_1\left(a_2\pm\sqrt{(r^2+3)^2-a_3^2}\right)}{2(a_4-(r^2+3)^2)} \tag{30}$$

For infinitesimal mesh spacing we have

$$\omega_1=\omega_{\mathrm{AN}}^{\mathrm{R}}+O(h^2),\quad \omega_2=\tfrac{1}{24}\beta kh^2+O(h^4)$$

4.3. The $P_1^{\mathrm{NC}}-P_1$ pair

4.3.1. Gravity modes. On Mesh 1, the selected discrete equations are expressed in the matrix form

$$\begin{pmatrix} A & 0 & 0 & \\ 0 & A & 0 & -gB^* \\ 0 & 0 & A & \\ & HB & & -3\mathrm{i}\omega \end{pmatrix}\begin{pmatrix}\tilde{\mathbf{u}}_H\\ \tilde{\mathbf{u}}_V\\ \tilde{\mathbf{u}}_D\\ \tilde{\boldsymbol{\eta}}_S\end{pmatrix}=0 \tag{31}$$

where $B=1/h(b_1\ \ b_2\ \ b_3\ \ b_4\ \ b_5\ \ b_6)$, with

$$b_1=2\mathrm{i}\sin\frac{kh}{2},\quad b_2=2\mathrm{i}\sin\frac{lh}{2}\cos\frac{(k-l)h}{2},\quad b_3=2\mathrm{i}\sin\frac{kh}{2}\cos\frac{(k-l)h}{2}$$

$$b_4=2\mathrm{i}\sin\frac{lh}{2},\quad b_5=2\mathrm{i}\sin\frac{kh}{2}\cos\frac{lh}{2},\quad b_6=2\mathrm{i}\sin\frac{lh}{2}\cos\frac{kh}{2}$$

Vanishing the 7×7 determinant in the left-hand side of (31) leads to $\omega_{1,2,3,4,5}=0$ and

$$\omega_{6,7}=\pm\sqrt{\frac{4}{3}\frac{gH}{h^2}\left(\cos^2\frac{(k-l)h}{2}\left(\sin^2\frac{kh}{2}+\sin^2\frac{lh}{2}\right)+2\left(1-\cos^2\frac{kh}{2}\cos^2\frac{lh}{2}\right)\right)} \tag{32}$$

For infinitesimal mesh spacing we have $\omega_{6,7}=\omega_{\mathrm{AN}}^{\mathrm{G}}+O(h^2)$.

On Mesh 2 we let

$$b_1=\frac{\mathrm{i}}{\sqrt{3}}\sin\frac{kh}{2},\quad b_3=\frac{\mathrm{i}}{\sqrt{3}}\sin\frac{kh}{2}\cos\frac{(k+\sqrt{3}l)h}{4}$$

$$b_4=\frac{\mathrm{i}}{6}\left(3\sin\frac{(-k+\sqrt{3}l)h}{4}+\sin\frac{(3k+\sqrt{3}l)h}{4}\right)$$

DOI: 10.1002/fld

$$b_2=\frac{\mathrm{i}}{3}\sin\frac{\sqrt{3}lh}{2},\quad b_5=\frac{\mathrm{i}}{\sqrt{3}}\sin\frac{kh}{2}\cos\frac{(k-\sqrt{3}l)h}{4}$$

$$b_6=\frac{\mathrm{i}}{6}\left(3\sin\frac{(k+\sqrt{3}l)h}{4}+\sin\frac{(-3k+\sqrt{3}l)h}{4}\right)$$

and we obtain

$$\omega_{6,7}=\pm 2\frac{\sqrt{gH}}{h}\sqrt{-\sum_{j=1}^{6}b_j^2} \tag{33}$$

with $\omega_{6,7}=\omega_{\mathrm{AN}}^{\mathrm{G}}+O(h^2)$ for infinitesimal mesh spacing.

4.3.2. Rossby modes. We let

$$a_1=2\sin kh+\sin lh+\sin(k-l)h$$

$$a_2=8\left(\cos^2\frac{(k-l)h}{2}\left(\sin^2\frac{kh}{2}+\sin^2\frac{lh}{2}\right)+2\left(1-\cos^2\frac{kh}{2}\cos^2\frac{lh}{2}\right)\right)$$

and obtain on Mesh 1

$$\frac{\omega}{\beta h}=\frac{-2a_1}{24r^2+a_2} \tag{34}$$

For infinitesimal mesh spacing we have

$$\omega=\omega_{\mathrm{AN}}^{\mathrm{R}}+O(h^2) \tag{35}$$

On Mesh 2, made up of equilateral triangles, Equations (34) and (35) are obtained but with

$$a_1=2\sin kh+2\sin\frac{kh}{2}\cos\frac{\sqrt{3}lh}{2}$$

$$a_2=16-4\cos kh-\frac{4}{3}\cos\sqrt{3}lh-8\cos\frac{kh}{2}\cos\frac{\sqrt{3}lh}{2}-\frac{8}{3}\cos\frac{3kh}{2}\cos\frac{\sqrt{3}lh}{2}$$

Note that the superconvergence ($O(h^4)$) obtained in [13, 14] for both the gravity and Rossby waves is lost when the mass matrix is lumped.

4.4. The P_1 iso P_2-P_1 pair

4.4.1. Gravity modes. On Mesh 1, the selected discrete equations lead to

$$\begin{pmatrix} A & 0 & 0 & 0 & \\ 0 & A & 0 & 0 & \\ & & & & -gB^* \\ 0 & 0 & A & 0 & \\ 0 & 0 & 0 & A & \\ & HB & & & -4\mathrm{i}\omega \end{pmatrix}\begin{pmatrix} \tilde{\mathbf{u}}_S \\ \tilde{\mathbf{u}}_H \\ \tilde{\mathbf{u}}_V \\ \tilde{\mathbf{u}}_D \\ \tilde{\eta}_S \end{pmatrix}=0 \tag{36}$$

DOI: 10.1002/fld

where $B=1/h(b_1\ \ b_2\ \ b_3\ \ b_4\ \ b_5\ \ b_6\ \ b_7\ \ b_8)$, with

$$b_1=\frac{\mathrm{i}}{3}(2\sin kh+\sin lh+\sin(k-l)h),\quad b_5=\mathrm{i}\left(\sin\frac{lh}{2}+\sin\frac{(2k-l)h}{2}\right)$$

$$b_2=\frac{\mathrm{i}}{3}(2\sin lh+\sin kh-\sin(k-l)h),\quad b_6=2\mathrm{i}\sin\frac{lh}{2}$$

$$b_3=2\mathrm{i}\sin\frac{kh}{2},\quad b_7=\mathrm{i}\left(\sin\frac{(k-l)h}{2}+\sin\frac{(k+l)h}{2}\right)$$

$$b_4=\mathrm{i}\left(\sin\frac{kh}{2}-\sin\frac{(k-2l)h}{2}\right),\quad b_8=\mathrm{i}\left(\sin\frac{(k+l)h}{2}-\sin\frac{(k-l)h}{2}\right)$$

The 9×9 determinant of the coefficient matrix above must vanish to obtain a non-trivial solution, and this leads to $\omega_{1,2,3,4,5,6,7}=0$ and

$$\omega_{8,9}=\pm\frac{\sqrt{gH}}{2h}\sqrt{-\sum_{j=1}^{8}b_j^2} \tag{37}$$

For infinitesimal mesh spacing we have $\omega_{8,9}=\omega_{\mathrm{AN}}^{\mathrm{G}}+O(h^2)$.

4.4.2. Rossby modes. We let

$$\begin{aligned}a_1 &= 338\sin kh+166\sin lh+163\sin(k-l)h\\ &\quad +2\sin 2kh+\sin 2lh+\sin 2(k-l)h+18\sin(2k-l)h+15\sin(k+l)h\\ a_2 &= 1248-488(\cos kh+\cos lh)+208(\cos(k-l)h-\cos(k+l)h)\\ &\quad -40\cos 2kh-40\cos 2lh-88\cos(2k-l)h-88\cos(k-2l)h-16\cos 2(k-l)h\end{aligned}$$

and on Mesh 1 we obtain

$$\frac{\omega}{\beta h}=\frac{-a_1}{2304r^2+a_2} \tag{38}$$

which reduces to

$$\omega=\frac{31}{32}\frac{-\beta k}{k^2+l^2+\lambda^{-2}}+O(h^2) \tag{39}$$

for infinitesimal mesh spacing.

5. ANALYSIS OF THE DISPERSION RELATIONS

5.1. Gravity wave limit

We now analyse the computed frequencies, denoted by $\omega_{\mathrm{CP}}^{\mathrm{G}}$, corresponding to the discrete gravity modes obtained for the four FE pairs described in Section 4. The expressions for $\omega_{\mathrm{CP}}^{\mathrm{G}}$ are obtained

DOI: 10.1002/fld

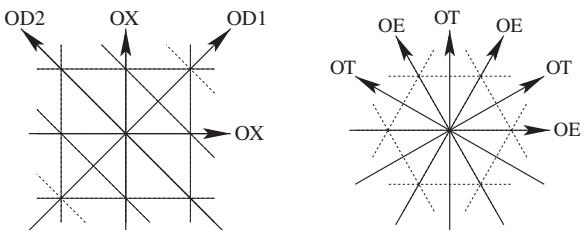

Figure 2. Definition of the selected axes OX, OY, $OD1$ and $OD2$ on Mesh 1 (left), and OE and OT on Mesh 2 (right).

from (24), (28), (32)–(33) and (37) for the P_0-P_1, RT_0, $P_1^{\mathrm{NC}}-P_1$ and P_1 iso P_2-P_1 pairs, respectively. Let ρ^{G} be the phase speed ratio of the computed phase speed to the analytical one, with

$$\rho^{\mathrm{G}} \equiv \frac{|\omega_{\mathrm{CP}}^{\mathrm{G}}|}{|\omega_{\mathrm{AN}}^{\mathrm{G}}|} = \frac{|\omega_{\mathrm{CP}}^{\mathrm{G}}|}{\sqrt{gH(k^2+l^2)}} \tag{40}$$

We show ρ^{G} as a surface function depending on kh and lh, and along selected axes, in Figures 3 and 4 for the FE schemes examined here. Note that we should have $\rho^{\mathrm{G}}=1$ in the absence of numerical dispersion. The selected axes OX, OY, $OD1$ and $OD2$ on Mesh 1, and OE and OT on Mesh 2 are shown in Figure 2. As in [10, 13], the values of kh and lh vary over the complete spectral domain $[-\pi, \pi]$. However, the phase speed ratio along the selected axes OX, OY, $OD1$, $OD2$ and OE is only plotted on $[0, \pi]$ and the solution is then deduced on $[-\pi, 0]$ by symmetry through the origin. Along the OT axis, ρ^{G} is plotted on $[0, \pi/\alpha]$, where $\alpha=\sqrt{3}/2$.

The phase speed ratio is plotted in Figure 3 for the P_0-P_1, $P_1^{\mathrm{NC}}-P_1$ and P_1 iso P_2-P_1 pairs on Mesh 1, and in Figure 4 for the RT_0 and $P_1^{\mathrm{NC}}-P_1$ pairs on Mesh 2. Along the selected axes, ρ^{G} is shown with (ML) and without (NML) the use of a mass lumping technique.

In Figure 3, the effect of the mass lumping technique is to damp all FE frequencies. The damping is more severe in the $OD2$ direction although $\rho^{\mathrm{G}} \geqslant 1$ in such a direction without lumping. We obtain $\rho^{\mathrm{G}} \leqslant 1$ for all values of kh and lh. Hence, the waves are travelling slower than expected, and this is particularly true for large values of $|kh|$ and $|lh|$. The damping effect is comparable for the $P_1^{\mathrm{NC}}-P_1$ and P_1 iso P_2-P_1 pairs, with slightly better results for the P_0-P_1 pair.

In Figure 4 on Mesh 2, the results for the $P_1^{\mathrm{NC}}-P_1$ pair are close to those obtained in Mesh 1 by taking into account that along the OT axis, ρ^{G} is plotted on $[0, \pi/\alpha]$. Much better results are observed for the RT_0 pair, particularly along the OE and OT directions where the NML and NL curves are in close agreement, even for large wave numbers.

5.2. *Rossby modes*

The computed frequencies corresponding to the discrete Rossby modes obtained in Section 4 for the four FE pairs examined here are now analysed. The expression for $\omega_{\mathrm{CP}}^{\mathrm{R}}$ is obtained from (25), (30), (34) and (38) for the P_0-P_1, RT_0, $P_1^{\mathrm{NC}}-P_1$ and P_1 iso P_2-P_1 pairs, respectively. We denote by ρ^{R} the ratio of the computed frequency to the analytical one and $\omega_{\mathrm{AN}}^{\mathrm{R}}$ is rewritten

DOI: 10.1002/fld

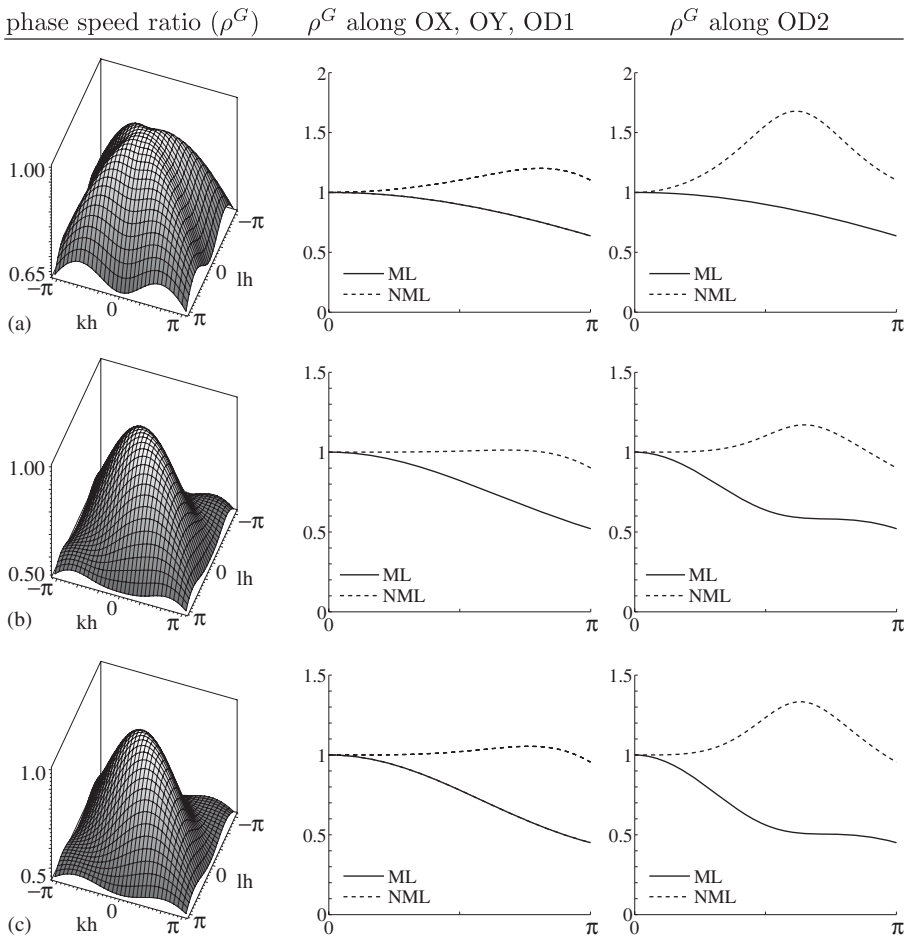

Figure 3. The phase speed ratio (ρ^{G}) is plotted as a surface function and along selected axes (OX, OY, $OD1$ and $OD2$) on Mesh 1 for the (a) P_0-P_1, (b) $P_1^{\mathrm{NC}}-P_1$ and (c) P_1 iso P_2-P_1 pairs. Along the selected axes, ρ^{G} is plotted with (ML) and without (NML) the use of mass lumping technique.

from (14) as

$$\rho^{\mathrm{R}} \equiv \frac{\omega_{\mathrm{CP}}^{\mathrm{R}}}{\omega_{\mathrm{AN}}^{\mathrm{R}}}, \quad \frac{\omega_{\mathrm{AN}}^{\mathrm{R}}}{\beta h} = \frac{-kh}{4r^2+(kh)^2+(lh)^2} \tag{41}$$

Again we should have $\rho^{\mathrm{R}}=1$ in the absence of numerical dispersion.

We show ρ^{R} by using contour levels depending on kh and lh in Figures 5 and 6 for the FE schemes previously examined. Following [25], three values of r are used: $r^2=0.1$, 1 and 10, corresponding to meshes ranging from fine ($r^2=0.1$) to coarse ($r^2=10$) resolution. The parameter r^2 measures the relative importance of the terms in the denominator of (25), (30), (34) and (38) when the wave scale is small.

DOI: 10.1002/fld

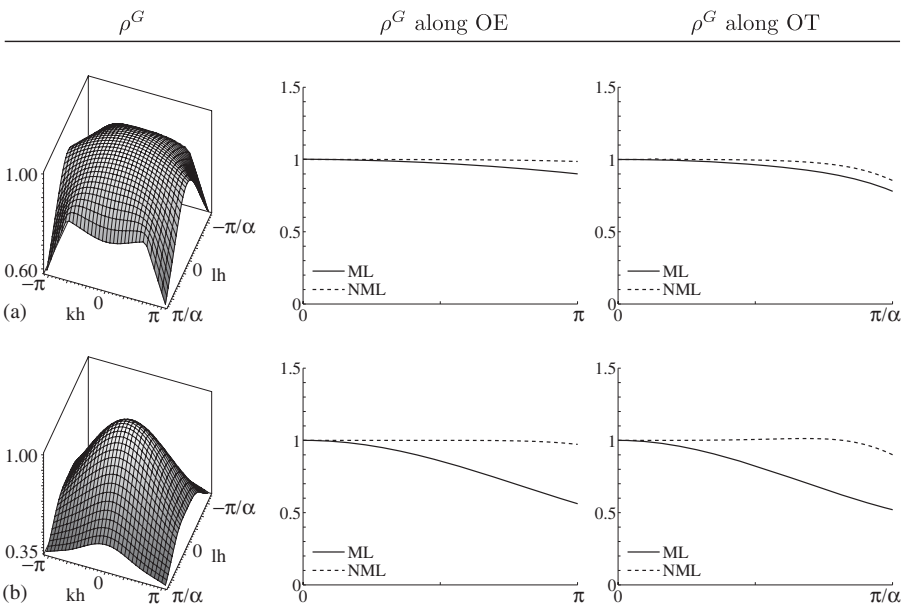

Figure 4. As for Figure 3 but for the (a) RT_0 and (b) $P_1^{NC}-P_1$ pairs on Mesh 2.

In Figure 5, the analytical and FE computed solutions agree well ($\rho^R \simeq 1$) for small-to-medium range wave numbers. Note that the region where $\rho \simeq 1$ is larger for the $P_1^{NC}-P_1$ and P_1 iso P_2-P_1 pairs than for the P_0-P_1 pair for $r^2=0.1$. However, for $kh=0$ and $lh=0$ we obtained the values $\rho^R=0.969$ from (39) for the P_1 iso P_2-P_1 pair, and thus the waves travel slower than expected for this pair. At the vicinity of $(kh=-\pi, lh=\pi/2)$ and $(kh=\pi, lh=-\pi/2)$ we have $\rho^R<0$ for all pairs, whatever the value of r^2, and the waves will thus decelerate.

In Figure 6 on Mesh 2, much better results are obtained for the RT_0 pair since ρ^R is closer to 1 over the greater part of the spectral domain. However, at the vicinity of $kh=0$ and $lh=\pm\pi/\alpha$, we have $\rho^R>1$ and the waves will thus accelerate, particularly for small values of r^2. For the $P_1^{NC}-P_1$ pair the results are similar to those obtained in Figure 5, except that the region where the waves decelerate is now located at the four corners of the spectral domain.

The two discrete frequencies obtained in (30) for the RT_0 scheme are plotted in Figure 7 and compared with the continuous solution ω_{AN}^R. The mode ω_2 in (30) is spurious whereas the mode ω_1 is well represented. Note that the origin of ω_2 is found in the coupling between the discrete momentum and continuity equations in SW models, and is not due to the mass lumping technique. Further, the impact of ω_2 on the numerical solution is still unclear.

6. NUMERICAL RESULTS

The results of three numerical tests examining the propagation and dispersion of fast gravity and slow Rossby waves are now presented for the four FE pairs employed in this paper. In addition to Meshes 1 and 2, we also consider Mesh 3, an unstructured mesh with smoothing.

DOI: 10.1002/fld

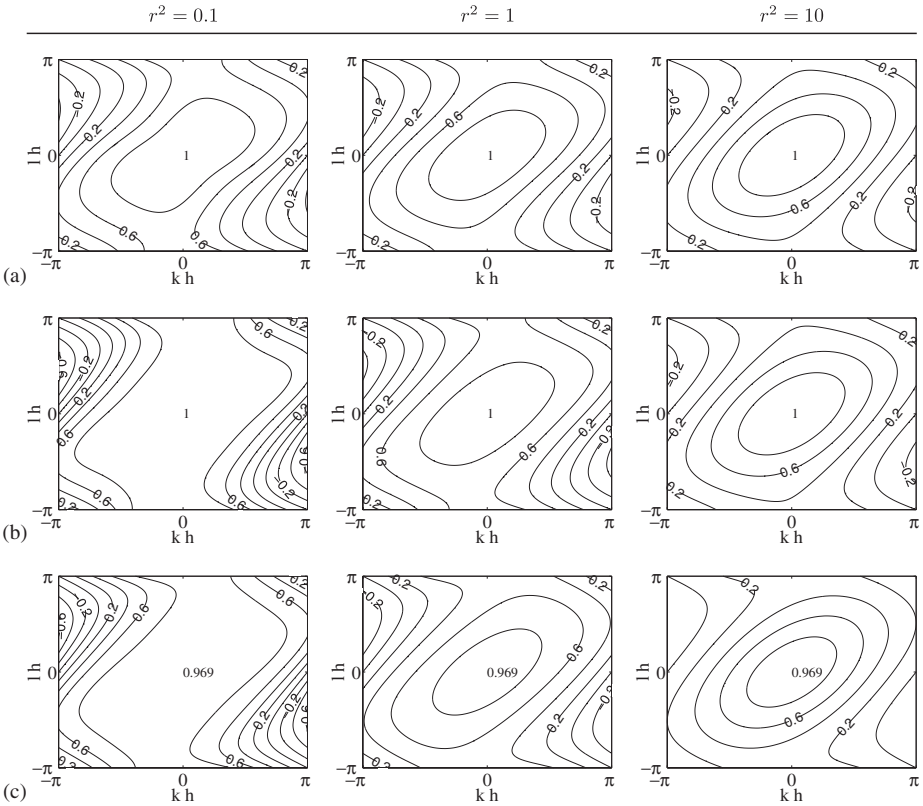

Figure 5. Contour levels of ρ^{R} for the (a) $P_0 - P_1$, (b) $P_1^{\mathrm{NC}} - P_1$ and (c) P_1 iso $P_2 - P_1$ on Mesh 1. Three values of r are used, $r^2 = 0.1$, 1 and 10, corresponding to meshes ranging from fine ($r^2 = 0.1$) to coarse ($r^2 = 10$) resolution.

6.1. Gravity waves

The domain is an idealized $L_x \times L_y$ rectangular basin discretized using $h = 40\,\mathrm{km}$. We let $L_x = 4800\,\mathrm{km}$, $L_y = 280\,\mathrm{km}$, and hence the mesh has 120 and 7 elements in the x- and y-directions, respectively. The origin of the domain is chosen to be the bottom left corner. The initial solution

$$\bar{\mathbf{u}} = 0 \tag{42}$$

$$\bar{\eta} = \cos(kx) \tag{43}$$

satisfies the no-normal flow boundary condition at lateral boundaries and periodic conditions are applied along the eastern and western boundaries.

The wave number k considered in the sequel (the wave moves in the x-direction) is such that $k = 2\pi v / L_x$, where v is defined as the length L_x over the wavelength. In the following we evaluate k for $v = 2, 3, 4, 5, 6, 8, 10, 12, 15, 20, 24, 30, 40, 60$. At each time step the elevation is computed at the centre of the domain $(L_x/2, L_y/2)$ and at the end of the simulation the time evolution of η at this point is obtained. By estimating the distance between the two nearest maxima the period T

DOI: 10.1002/fld

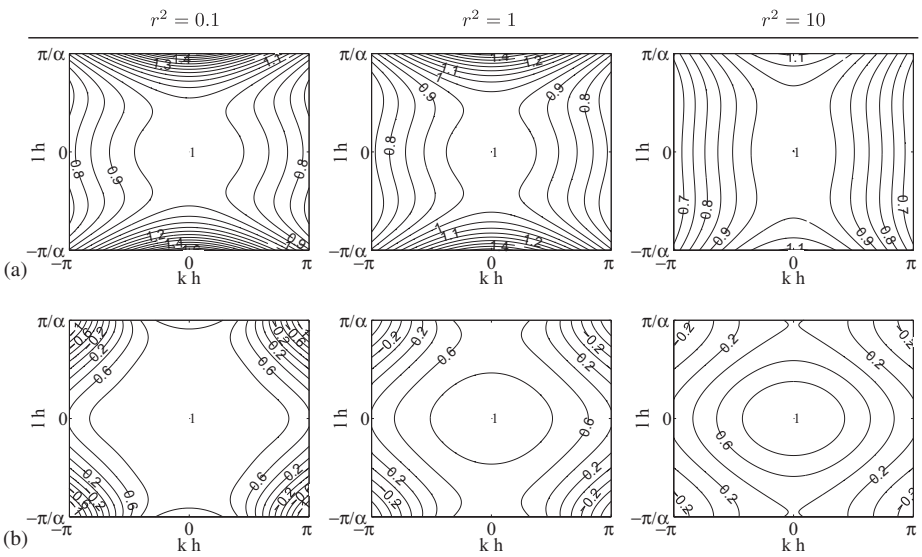

Figure 6. As for Figure 5 but for the (a) RT_0 and (b) $P_1^{NC} - P_1$ pairs on Mesh 2.

and the frequency $\omega = 2\pi/T$ are then deduced for each value of k. The choices $g = 10\,\mathrm{m\,s^{-2}}$ and $H = 1000\,\mathrm{m}$ result in a phase speed for gravity waves of $100\,\mathrm{m\,s^{-1}}$. The time step is set to 20 s and the simulation is carried on for 5000 time steps. A Crank–Nicolson scheme is used for the gradient and divergence operators.

In Figure 8, the effect of mass lumping appears to be the same for all FE pairs on both Meshes 1 and 3 (the RT_0 element is not included here). It leads to a reduction in the discrete frequency for small wavelengths. As a result, the modes with a wavelength smaller than $4h$ are slowed down by the numerical scheme whereas the others remain mostly unaffected. For the RT_0 pair, the curves for the consistent (NML) and lumped (ML) schemes are in close agreement in Figure 9, even for large wave numbers. The $P_1^{NC} - P_1$ pair is found to give similar results and damping on Meshes 1 and 2. Note that the discrete analytical (ω_{CP}^{G}) and numerically simulated dispersion relations (when available) nearly coincide for all pairs.

6.2. *Rossby waves*

The results of two numerical tests are presented. The first experiment examines the propagation and dispersion of slow propagating Rossby modes in the case of the evolution of a typical anticyclonic eddy at midlatitudes. In the second test, the experiment conducted in Section 6.1 for gravity waves is performed for Rossby waves.

6.2.1. Anticyclonic eddy propagation. The domain of interest is an idealized $2000\,\mathrm{km} \times 1200\,\mathrm{km}$ rectangular basin and h is set to 20 km. Equations (1)–(2) are solved subject to the no-normal flow boundary condition $\bar{\mathbf{u}} \cdot \mathbf{n} = 0$. A Gaussian distribution of $\bar{\eta}$, centred at the origin of the domain, is prescribed at initial time, and the initial symmetric anticyclonic velocity field is in geostrophic

DOI: 10.1002/fld

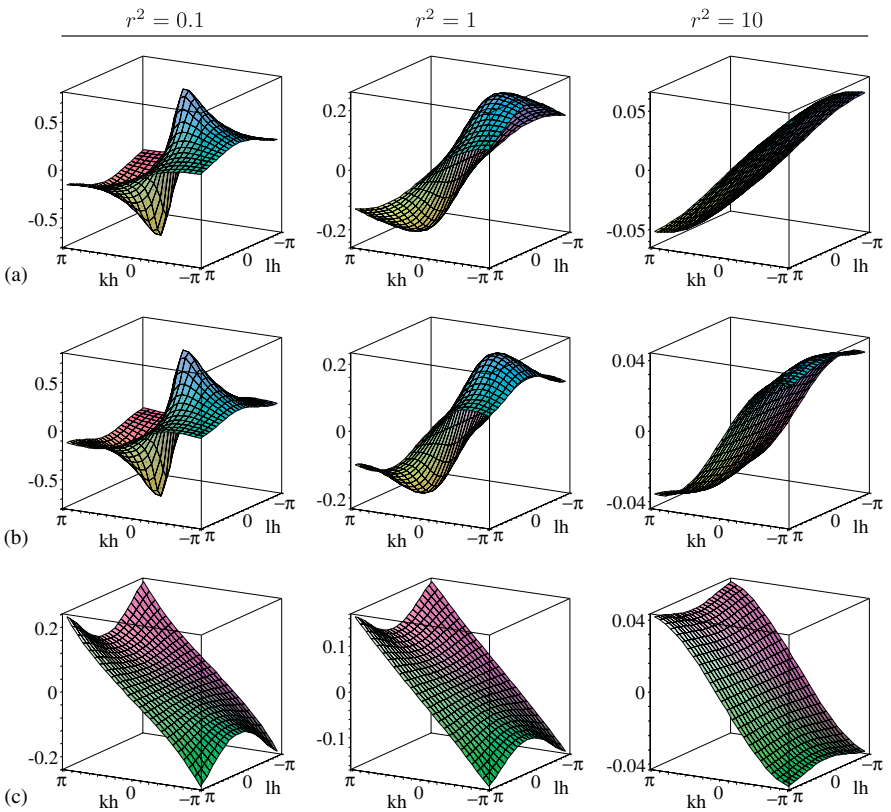

Figure 7. The frequency for the Rossby modes is plotted as a surface function for the (a) continuous case ($\omega_{\mathrm{AN}}^{\mathrm{R}}$) and the two discrete frequencies obtained in (30) for the RT_0 scheme (b) ω_1 and (c) ω_2. Three values of r are used, $r^2 = 0.1$, 1 and 10, corresponding to meshes ranging from fine ($r^2 = 0.1$) to coarse ($r^2 = 10$) resolution.

balance: $f\mathbf{k}\times\bar{\mathbf{u}} = -g\nabla\bar{\eta}$, and thus

$$\bar{\eta} = A\mathrm{e}^{-(x^2+y^2)/B^2} \tag{44}$$

$$\bar{u} = 2A\frac{g}{f_0+\beta y}\frac{y}{B^2}\mathrm{e}^{-(x^2+y^2)/B^2} \tag{45}$$

$$\bar{v} = -2A\frac{g}{f_0+\beta y}\frac{x}{B^2}\mathrm{e}^{-(x^2+y^2)/B^2} \tag{46}$$

By setting $A = 0.95\,\mathrm{m}$ and, for example, $B = 130\,\mathrm{km}$, the initial maximum surface azimuthal velocity is $1\,\mathrm{m\,s^{-1}}$. The constant depth $H = 1.631\,\mathrm{m}$ results in a phase speed for gravity waves of approximately $4\,\mathrm{m\,s^{-1}}$. Such a small equivalent depth is pertinent for the adjustment under gravity of a density-stratified fluid [17]. The β-plane approximation, $f = f_0 + \beta y$, is used, where f_0 and β are evaluated at 25°N ($f_0 = 6.1635\times10^{-5}\,\mathrm{s^{-1}}$ and $\beta = 2.0746\times10^{-11}\,\mathrm{m^{-1}\,s^{-1}}$). The radius of

DOI: 10.1002/fld

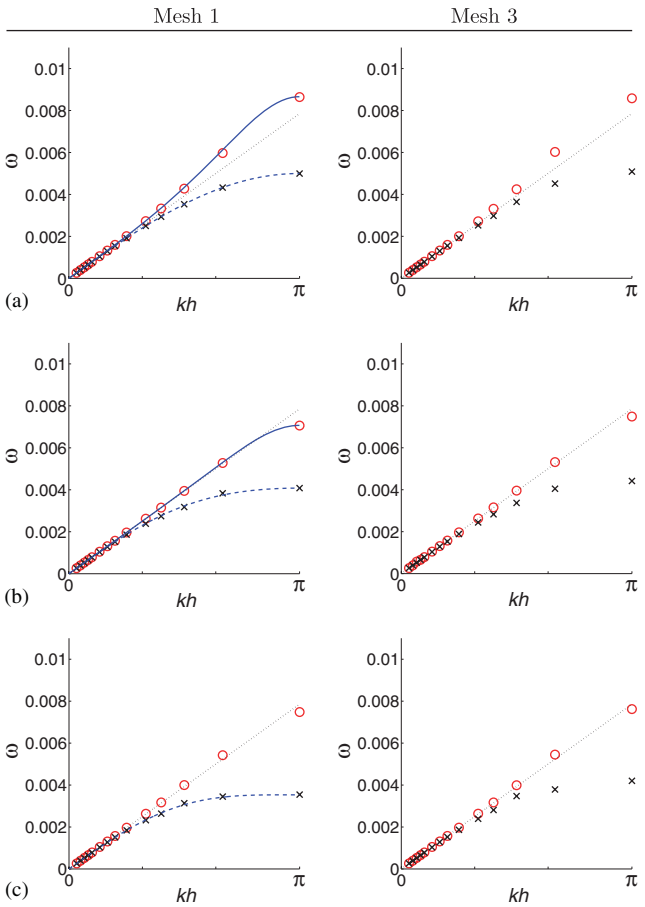

Figure 8. Continuous analytical (ω^{G}_{AN}, dotted line), discrete analytical (ω^{G}_{CP}, solid and dashed lines for NML and ML, respectively, when available) and numerically simulated ($\circ$ and $\times$ for NML and ML, respectively) dispersion relations for gravity waves and for the (a) P_0-P_1, (b) $P_1^{NC}-P_1$ and (c) P_1 iso P_2-P_1 pairs on Meshes 1 and 3.

deformation at midbasin is thus $\lambda \equiv \sqrt{gH}/f_0 \approx 65\,\text{km}$. The time step is 1800 s and Equations (1)–(2) are discretized in time using the Crank–Nicholson scheme.

After the initial condition adjusts to the β-plane balance of the model, the anticyclonic vortex evolves purely westward. After few weeks of simulation the surface elevation and flow speed field are close to the results obtained in [14] without the use of the mass lumping technique.

More quantitative results are obtained in Table I by considering the number of time steps it takes for the initial surface elevation to propagate over 100 km. We still have $A=0.95$ and the parameter B is chosen to be $B=60, 80, 100$ and 120 km, so that the e-folding radius of the initial Gaussian (the distance from the origin for which $\bar{\eta}=e^{-1}$) is resolved by $3, 4, 5$ and 6 nodes, respectively, in the x-direction. The results are obtained on Meshes 1 and 2, without (NML) and with (ML) the use of the mass lumping technique. For each FE pair the number of time steps is indicated in

DOI: 10.1002/fld

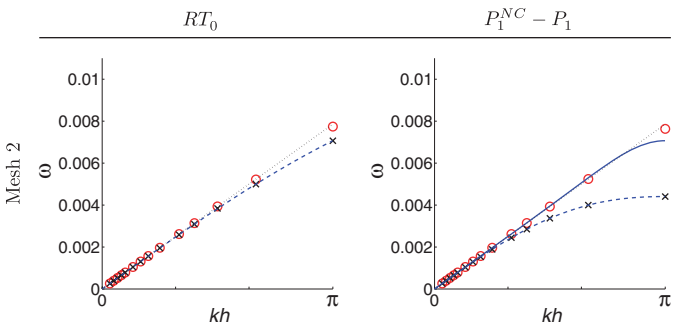

Figure 9. As for Figure 8 but on Mesh 2 for the RT_0 and $P_1^{NC} - P_1$ pairs.

Table I. The number of time steps it takes for the initial surface elevation to propagate over 100 km on Meshes 1 and 2.

		$B = 60$ km		$B = 80$ km		$B = 100$ km		$B = 120$ km	
FE	Mesh	NML	ML	NML	ML	NML	ML	NML	ML
$P_0 - P_1$	1	3298	+47	2320	+24	1810	+18	1497	+12
	2	3245	+34	2285	+20	1792	+12	1487	+9
RT_0	2	3191	+1	2287	+3	1810	+1	1504	−1
$P_1^{NC} - P_1$	1	3315	+51	2310	+23	1803	+13	1492	+12
	2	3252	+41	2290	+18	1791	+15	1487	+8
P_1 iso $P_2 - P_1$	1	3283	+133	2303	+43	1799	+24	1490	+19
	2	3227	+78	2275	+33	1782	+22	1479	+14

For each FE pair and several values of B, the number of time steps is indicated in column NML (no mass lumping), whereas in column ML (mass lumping) the positive or negative number needs to be added to the NML result to obtain the number of time steps for the ML case.

column NML, whereas in column ML the positive or negative number needs to be added to the NML result to obtain the number of time steps for the ML case. The numbers in column ML thus represent the delay (if positive) or advance (if negative) expressed in time steps of the lumped solution compared with the consistent one (not lumped).

For the RT_0 scheme, the mass lumping technique has practically no effect on the propagation speed of the eddy, whatever the choice of B. For the three other pairs, the ML solution progresses slower than the NML one on both meshes, and the delay increases with decreasing values of B. The delay is significant for the P_1 iso $P_2 - P_1$ pair, particularly for small B, and it may be regarded as a consequence of (39). Common to the $P_0 - P_1$, $P_1^{NC} - P_1$ and P_1 iso $P_2 - P_1$ pairs is a smaller delay on Mesh 2 than on Mesh 1.

6.2.2. Propagation of slow modes in a canal. The test performed in Section 6.1 is reproduced here in the context of the propagation of slow Rossby modes. The experiment is unchanged except

DOI: 10.1002/fld

that the initial solution

$$\bar{u} = -\frac{gl}{f}\cos(kx)\cos(ly) \tag{47}$$

$$\bar{v} = -\frac{gk}{f}\sin(kx)\sin(ly) \tag{48}$$

$$\bar{\eta} = \cos(kx)\sin(ly) \tag{49}$$

where $l = \pi/L_y$ is now in geostrophic balance and still satisfies the no-normal flow boundary condition at lateral boundaries. Further, two values of L_y are considered. For the $P_0 - P_1$, RT_0 and $P_1^{\mathrm{NC}} - P_1$ pairs, L_y is set to 280 km as this value was found sufficient in [14, 26] to well approximate the Rossby waves (without the mass lumping technique). This is due to the small smallest representable vortices (SRV) structure found for the three pairs in [26], where the SRV are defined as the elements of the discrete Coriolis, divergence and gradient matrix kernels with minimum support. In [26], the size and structure of the SRV are compared for several FE pairs on local mesh patches. It is shown that the $P_0 - P_1$, RT_0 and $P_1^{\mathrm{NC}} - P_1$ pairs can characterize smaller SRV structures efficiently and with less oscillatory behaviour than the P_1 iso $P_2 - P_1$ pair, for example. For the P_1 iso $P_2 - P_1$ pair, larger SRV are found in [26], and hence a larger L_y was needed (840 km) to compute the slow modes. This is why $L_y = 840$ km is employed in the present experiment for the last pair. Periodic conditions are again applied along the eastern and western boundaries. The β-plane approximation, $f = f_0 + \beta y$, is used where $f_0 = 10^{-4}\,\mathrm{s}^{-1}$ and $\beta = 10^{-11}\,\mathrm{m}^{-1}\,\mathrm{s}^{-1}$. By setting $g = 0.1\,\mathrm{m\,s}^{-2}$ and $H = 1000$ m results in a phase speed for gravity waves of $10\,\mathrm{m\,s}^{-1}$. The radius of deformation at midbasin is thus $\lambda = 100$ km.

The wave number k is again such that $k = 2\pi\nu/L_x$ (the wave still moves in the x-direction) with $\nu = 2, 3, 4, 5, 6, 8, 10, 12, 15, 20, 24, 30, 40, 60$. The time step is set to 2×10^4 s and the duration of the simulation is 10^4 time steps. A Crank–Nicolson scheme is used for the Coriolis, gradient and divergence operators.

In Figures 10–12 close agreement is observed on Meshes 1 and 2 (when the results are available) between the consistent and lumped schemes for all pairs. The numerical results also closely match with the analytical dispersion relations obtained in the discrete case. On Mesh 3, the results for the $P_0 - P_1$, $P_1^{\mathrm{NC}} - P_1$ and RT_0 (shown in [26, Figure 5.5]) pairs are quite good. However, significant errors are observed in Figure 12 for the P_1 iso $P_2 - P_1$ pair on such a mesh. This may be due to the absence of SRV for this pair on unstructured meshes as shown in [26], and both the consistent and lumped frequencies are not accurately computed.

7. CONCLUDING REMARKS

To our knowledge, the preceding analysis appears to be the first study of the effect of mass lumping on the dispersion relation for FE solutions of the 2-D SW equations based on the examination of a variety of mixed FE pairs. Four pairs are examined, and for each pair the lumped frequency is obtained and analysed for both the gravity and Rossby waves. The dispersion properties are also compared analytically and graphically with the continuous case. Three numerical tests, concerning the propagation of gravity and Rossby waves, are performed.

It is found that the FE schemes examined here are mostly unaffected by mass lumping as far as the propagation of gravity waves is concerned. Only the modes with a wavelength smaller than

DOI: 10.1002/fld

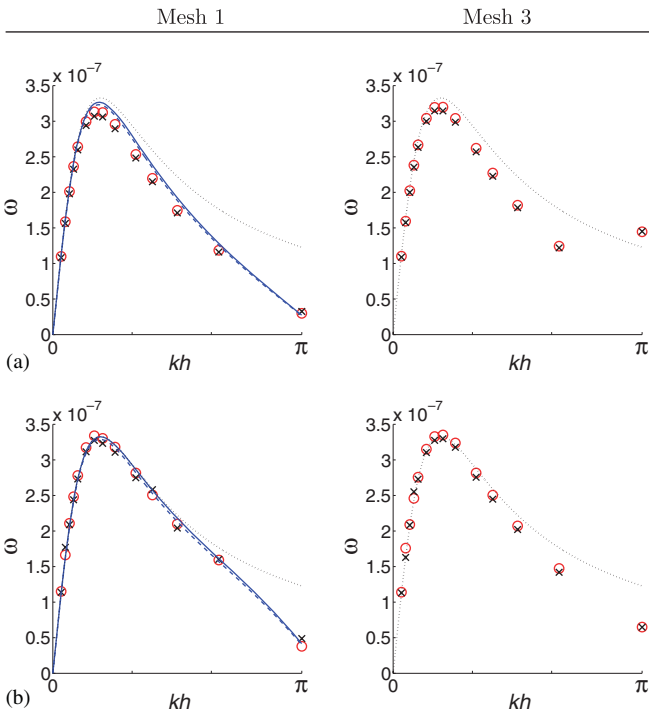

Figure 10. Continuous analytical ($\omega^{\mathrm{R}}_{\mathrm{AN}}$, dotted line), discrete analytical ($\omega^{\mathrm{R}}_{\mathrm{CP}}$, solid and dashed lines for NML and ML, respectively, when available) and numerically simulated ($\circ$ and $\times$ for NML and ML, respectively) dispersion relations for Rossby waves and for the (a) $P_0 - P_1$ and (b) $P_1^{\mathrm{NC}} - P_1$ pairs on Meshes 1 and 3, with $L_y = 280\,\mathrm{km}$.

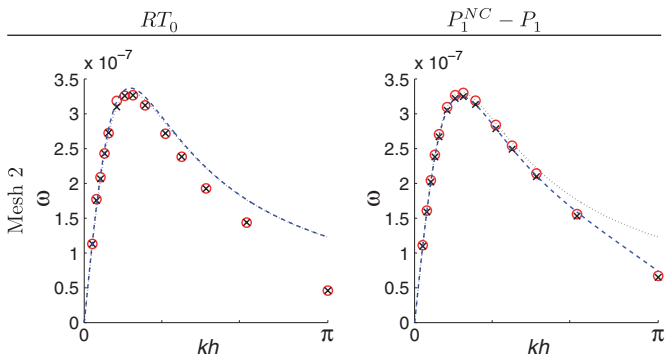

Figure 11. As for Figure 10 but for the RT_0 and $P_1^{\mathrm{NC}} - P_1$ pairs on Mesh 2 with $L_y = 280\,\mathrm{km}$.

$4h$ are slowed down by the numerical schemes (with the exception of the RT_0 pair) whereas the others remain mostly unaffected.

However, the situation is different for the propagation of Rossby waves. For all pairs, except the RT_0 one, the lumped solution propagates slower than the consistent one, and the delay increases

DOI: 10.1002/fld

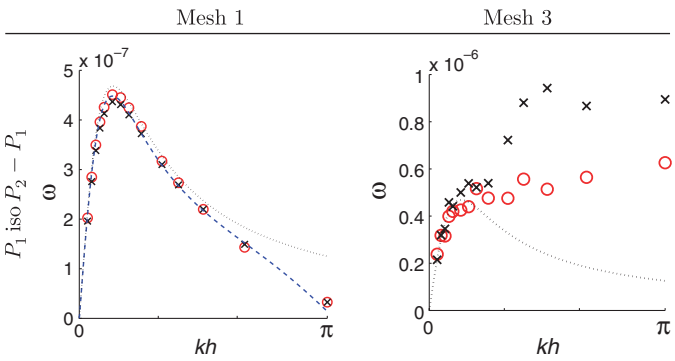

Figure 12. As for Figure 10 but for the P_1 iso $P_2 - P_1$ pair with $L_y = 840$ km.

as the mesh gets coarser. The P_1 iso $P_2 - P_1$ pair is mostly affected by the delay. On the other hand, the dispersion errors due to mass lumping remain small for the $P_0 - P_1$, RT_0 and $P_1^{\mathrm{NC}} - P_1$ pairs, with the exception of the smallest wavelength, on both regular and unstructured meshes. Significant errors are observed for the P_1 iso $P_2 - P_1$ pair on the latter mesh but this problem is not primarily due to the lumping technique. Finally, we note that the superconvergence obtained for the $P_1^{\mathrm{NC}} - P_1$ frequency for both gravity and Rossby waves with the consistent solution is lost when the mass matrix is lumped.

It thus appears that the $P_0 - P_1$, RT_0 and $P_1^{\mathrm{NC}} - P_1$ pairs can be advantageously lumped in SW simulations without sacrificing the model's accuracy and dispersion properties, for sufficiently fine resolution. The resulting model would then combine the advantages of both fast and simple finite-difference schemes, and unstructured and flexible FE ones.

ACKNOWLEDGEMENTS

This work is supported by grants to DYL from the Natural Sciences and Engineering Research Council (NSERC). EH thanks the Nuffield Foundation for a newly appointed lecturer award.

REFERENCES

1. Agoshkov V, Ovtchinnikov E, Pennati V, Ambrosi D, Saleri F. Finite element, finite volume and finite differences approximation to the shallow water equations. In *Finite Elements in Fluids*, Morgan K, Oñate E, Periaux J, Peraire J, Zienkiewicz OC (eds). Pineridge Press, 1993; 1001–1009.
2. Carey GF (ed.). *Finite Element Modeling of Environmental Problems*. Wiley: U.K., 1995.
3. Danilov S, Kivman G, Schröter J. A finite-element ocean model: principles and evaluation. *Ocean Modelling* 2004; **6**:125–150.
4. Iskandarani M, Haidvogel D, Boyd J. A staggered spectral finite-element model for the shallow-water equations. *International Journal for Numerical Methods in Fluids* 1995; **20**:393–414.
5. Lynch DR, Gray WG. A wave-equation model for finite-element tidal computations. *Computers and Fluids* 1979; **7**:207–228.
6. Walters RA. A three-dimensional finite-element model for coastal and estuarine circulation. *Continental Shelf Research* 1992; **12**:83–102.
7. Walters RA, Casulli V. A robust, finite-element model for hydrostatic surface water flows. *Communications in Numerical Methods in Engineering* 1998; **14**:931–940.

DOI: 10.1002/fld

8. Hinton E, Rock T, Zienkiewicz OC. A note on mass lumping and related processes in the finite element method. *Earthquake Engineering and Structural Dynamics* 1976; **4**:245–249.
9. Fried I, Malkus DS. Finite element mass matrix lumping by numerical integration with no convergence rate loss. *International Journal of Solids and Structures* 1975; **11**:461–466.
10. Foreman MGG. A two-dimensional dispersion analysis of selected methods for solving the linearized shallow-water equations. *Journal of Computational Physics* 1984; **56**:287–323.
11. Le Roux DY, Carey GF. Stability/dispersion analysis of the discontinuous Galerkin linearized shallow-water system. *International Journal for Numerical Methods in Fluids* 2005; **48**:325–347.
12. Le Roux DY. Dispersion relation analysis of the $P_1^{\mathrm{NC}} - P_1$ finite-element pair in shallow-water models. *SIAM Journal on Scientific Computing* 2005; **27**:394–414.
13. Le Roux DY, Rostand V, Pouliot B. Analysis of numerically-induced oscillations in 2D finite-element shallow-water models. Part I: inertia-gravity waves. *SIAM Journal on Scientific Computing* 2007; **29**:331–360.
14. Le Roux DY, Pouliot B. Analysis of numerically-induced oscillations in 2D finite-element shallow-water models. Part II: free planetary waves. *SIAM Journal on Scientific Computing* 2008; **30**(4):1971–1991.
15. Rostand V, Le Roux DY. Raviart–Thomas and Brezzi–Douglas–Marini finite element approximations of the shallow-water equations. *International Journal for Numerical Methods in Fluids* 2007. DOI: 10.1002/fld.1668.
16. LeBlond PH, Mysak LA. *Waves in the Ocean*. Elsevier: Amsterdam, 1978.
17. Gill AE. *Atmosphere-Ocean Dynamics*. International Geophysics Series, vol. 31. Academic Press: New York, 1982.
18. Longuet-Higgins MS. Planetary waves on a rotating sphere II. *Proceedings of the Royal Society of London* 1965; **284**:40–54.
19. Wentzel G. A generalization of quantum conditions for the purposes of wave mechanics. *Zeitschrift fur Physik* 1926; **38**:518–529.
20. Raviart P, Thomas J. A mixed finite element method for 2nd order elliptic problems. In *Mathematical Aspects of the Finite Element Methods*, Galligani I, Magenes E (eds). Lecture Notes in Mathematics. Springer: Berlin, 1977; 292–315.
21. Hua BL, Thomasset F. A noise-free finite-element scheme for the two-layer shallow-water equations. *Tellus* 1984; **36A**:157–165.
22. Bercovier M, Pironneau O. Error estimates for the finite element method solution of the Stokes problem in the primitive variables. *Numerische Mathematik* 1979; **33**:211–224.
23. Sigurdsson S. Treatment of the convective term in staggered finite element schemes for shallow water flow. In *Computational Methods in Water Resources IX*, *Vol. 1*: *Numerical Methods in Water Resources*, Russel TF, Ewing RE, Brebia CA, Gray WG, Pinder GF (eds). Computational Mechanics Publications, Elsevier Applied Science: 1992; 291–298.
24. Baranger J, Maitre JF, Oudin F. Connection between finite volume and mixed finite element methods. *Mathematical Modelling and Numerical Analysis* 1996; **30**:445–465.
25. Wajsowicz RC. Free planetary waves in finite-difference numerical models. *Journal of Physical Oceanography* 1986; **16**:773–789.
26. Rostand V, Le Roux DY, Carey G. Kernel analysis of the discretized finite difference and finite element shallow water models. *SIAM Journal on Scientific Computing* 2008; in press.